

Article

Secondary beams at high-intensity electron accelerator facilities

Marco Battaglieri¹, Andrea Bianconi^{2,3}, Mariangela Bondi⁴, Raffaella De Vita¹, Antonino Fulci^{4,5*}, Giulia Gosta², Stefano Grazzi^{1,5}, Hyon-Suk Jo⁶, Changhui Lee⁶, Giuseppe Mandaglio^{4,5}, Valerio Mascagna^{2,3}, Tetiana Nagorna¹, Alessandro Pilloni^{4,5}, Marco Spreafico^{1,7}, Luca J Tagliapietra⁸, Luca Venturelli^{2,3} and Tommaso Vittorini^{1,7}

¹ Istituto Nazionale di Fisica Nucleare, Sezione di Genova, 16146 Genova, Italy

² Istituto Nazionale di Fisica Nucleare, Sezione di Pavia, 27100 Pavia, Italy

³ Università degli Studi di Brescia, 25123 Brescia, Italy

⁴ Istituto Nazionale di Fisica Nucleare, Sezione di Catania, 95125 Catania, Italy

⁵ Università degli Studi di Messina, 98166 Messina, Italy

⁶ Kyungpook National University, Daegu 41566, Republic of Korea

⁷ Università degli Studi di Genova, 16126 Genova, Italy

⁸ NEVNUCLAB, 123 W Nye Lane, Carson City, Nevada, USA.

* Corresponding author: antonino.fulci@unime.it

Paper published on 3 May 2018 with minor changes in this version.

Abstract: The interaction of a high-current $O(100 \mu\text{A})$, medium energy $O(10 \text{ GeV})$ electron beam with a thick target $O(1\text{m})$ produces an overwhelming shower of standard model particles in addition to hypothetical Light Dark Matter particles. While most of the radiation (gamma, electron/positron) is contained in the thick target, deep penetrating particles (muons, neutrinos, and light dark matter particles) propagate over a long distance, producing high-intensity secondary beams. Using sophisticated Monte Carlo simulations based on FLUKA and GEANT4, we explored the characteristics of secondary muons and neutrinos and (hypothetical) dark scalar particles produced by the interaction of Jefferson Lab 11 GeV intense electron beam with the experimental Hall-A beam dump. Considering the possible beam energy upgrade, this study was repeated for a 22 GeV CEBAF beam.

Keywords: Intensity frontier, neutrino interaction, dark matter, BSM physics, muon beam

1. Introduction

High-intensity particle beams represent one of the current frontiers of discovery in particle and nuclear physics. High-intensity proton beams are routinely used to generate secondary beams of particles such as neutrinos and muons that could be used to extend the exploration of matter with new and different probes.

High-current ($\sim 100 \mu\text{A}$), medium-energy (1 GeV–10 GeV), continuous-wave electron beams with a delivered large integrated charge ($\sim 1000 \text{ C/y}$) can be also used to generate secondary beams. In fixed-target experiments, after the interaction with a thin target, the beam is dumped on a block of material where electrons produce showers, degrading the initial energy down to values at which ionization and excitation of atoms dominates. If the primary beam's initial energy is higher than the pion production threshold, hadronic interaction and electromagnetic processes contribute to the production of a sizable number of secondary particles that may re-interact or escape from the dump. The beam dump (BD) is usually surrounded by heavy shielding (e.g., a thick concrete vault) to minimize the escaping radiation. Nevertheless, a significant flux of neutrons, muons, and neutrinos propagate through the shielding, making intense secondary beams that may provide an opportunistic extension of investigations performed with the primary electromagnetic probe. According to recent

theoretical studies, the interaction of an intense electron beam with the beam dump could also be a source of a light dark matter (LDM) particle beam [1]. LDM particles are viable candidates to explain gravitational anomalies, extending the current set of elementary particles and interactions beyond the standard model (BSM).

The electron's prevalent electromagnetic interaction represents an alternative and complementary method of producing intense secondary beams that differ from hadronic-initiated reactions for the energy spectrum, the spatial dispersion, and the associated background. Using FLUKA and GEANT4, the state-of-the-art simulation tools widely used in high-energy and nuclear physics, we studied and characterized the secondary muons, neutrinos, and (hypothetical) LDM beams produced at the Jefferson Lab via the interaction of the primary electron beam with the experimental Hall-A BD. A similar study with higher energy lepton beams has been performed for the future ILC facility [2].

The paper is organized as follows: in Section 2, some details about the Thomas Jefferson National Accelerator Facility (Jefferson Lab or JLab) are reported. In Section 3, the simulation framework used to derive the secondary beams is described. Sections 4–6 report the expected characteristics of muon, neutrino, and LDM secondary beams. The conclusions and future outlook are reported in the last section.

2. The Thomas Jefferson National Accelerator Facility

The Jefferson Lab is a US Department of Energy laboratory located in Newport News, Virginia. JLab hosts the Continuous Electron Beam Accelerator Facility (CEBAF), a continuous wave (CW) electron accelerator, made by two 1-GeV LINACs and recirculating arcs to achieve, in five passes, the maximum energy. The machine started operations in 1994, delivering a 4 GeV beam, which was soon upgraded to 6 GeV and later to 12 GeV. At present, four experimental halls can receive, simultaneously, a primary 11 GeV electron beam (Hall-A, -B, and -C) and up to 12 GeV electron beam (Hall-D, then converted to a secondary photon beam) to conduct scattering experiments on nucleons and nuclei. The physics program includes the study of the hadron spectrum, nucleon structure, nuclear interaction, and BSM searches. The excellent quality of the polarized electron beam allows one to run high-precision parity-violation experiments that use the interference between electromagnetic and weak interaction to study the properties of quarks inside hadrons and nuclear matter. Hall-A and Hall-C are equipped with high-precision magnetic spectrometers. The detector's small acceptance requires high current (1–150 μA) on target to reach the typical luminosity of $10^{39} \text{ cm}^{-2}\text{s}^{-1}$. The high-current operations make Hall-A BD the ideal source of secondary beams at Jefferson Lab. The current BD configuration limits the maximum power to $<1 \text{ MW}$ corresponding to 90 μA current at 11 GeV beam energy or higher current at lower energy. High-current experiments with long durations are planned for Hall-A in the next decade, while the number of running days per year for Hall-C will be more sparse. Hall-B and Hall-D host two large-acceptance spectrometers (CLAS12 and GlueX) based on a toroidal (CLAS12) and solenoidal (GlueX) magnetic field. The almost 4π acceptance limits the current to hundreds of nA in Hall-B, and to a few μA in Hall-D's radiator (to generate a Bremsstrahlung real-photon beam). Dumps installed in these two halls are limited to a power of $\sim 100 \text{ kW}$, reducing the intensity of the incoming primary beam to values unsuitable for generating intense secondary beams. For this reason, we focused this study on the Hall-A beam dump only.

Currently, a study to increase the maximum beam energy of the CEBAF accelerator complex is underway. Taking advantage of progress in accelerator technologies, it will be possible to extend the energy reach of the CEBAF accelerator up to 22 GeV [3] within the current tunnel footprint and reusing the existing superconducting radio frequency (SRF) cavity system. Using the fixed-field alternating-gradient (FFA) technique, it will be possible to increase the number of passes through the accelerating cavities by reusing the same recirculating arcs. Considering the possibility of this upgrade, we studied the characteristics of secondary beams in the two configurations: the existing 11 GeV primary electron beam energy and a future 22 GeV.

3. The Simulation Framework

The interaction of the 11 GeV (22 GeV) primary electron beam with the Hall-A BD and subsequent transportation of the secondary muon, neutrino, and LDM beams was studied by Monte Carlo simulations using FLUKA [4,5] and GEANT4 [6] toolkits. The same simulation framework was successfully used to describe the results of the BDX-HODO [7] and BDX-MINI [8] experiments at Jefferson Lab.

3.1. FLUKA

FLUKA [9–12] version 4-3.1 was used to simulate the interaction of the primary electron beam with the Hall-A beam dump and the propagation of muons and neutrinos through concrete and dirt to reach a hypothetical downstream detector. The Hall-A beam dump geometry and materials were implemented according to the prescriptions of JLab Radiation Control Group [13].

The beam dump consists of approximately 80 aluminum disks, each with a diameter of roughly 40 cm. The disk thickness progressively increases from 1 cm to 2 cm, spanning a cumulative length of about 200 cm. Downstream of the disks, there is an aluminum cylinder, measuring 50 cm in diameter and approximately 100 cm in length. To ensure optimal temperature control, disks and cylinders are thermalized using a water-cooling circuit. To enhance the radiation shielding capabilities, the beam dump is surrounded by ~ 8 m of concrete in the longitudinal direction (where the high-energy secondary particles are produced) and about ~ 3 m of concrete in the transverse direction. Furthermore, the entire setup is covered by ~ 4 m of overburden. The BD, the beam transport line, and the surrounding concrete vault are shown (to scale) in Figure 1.

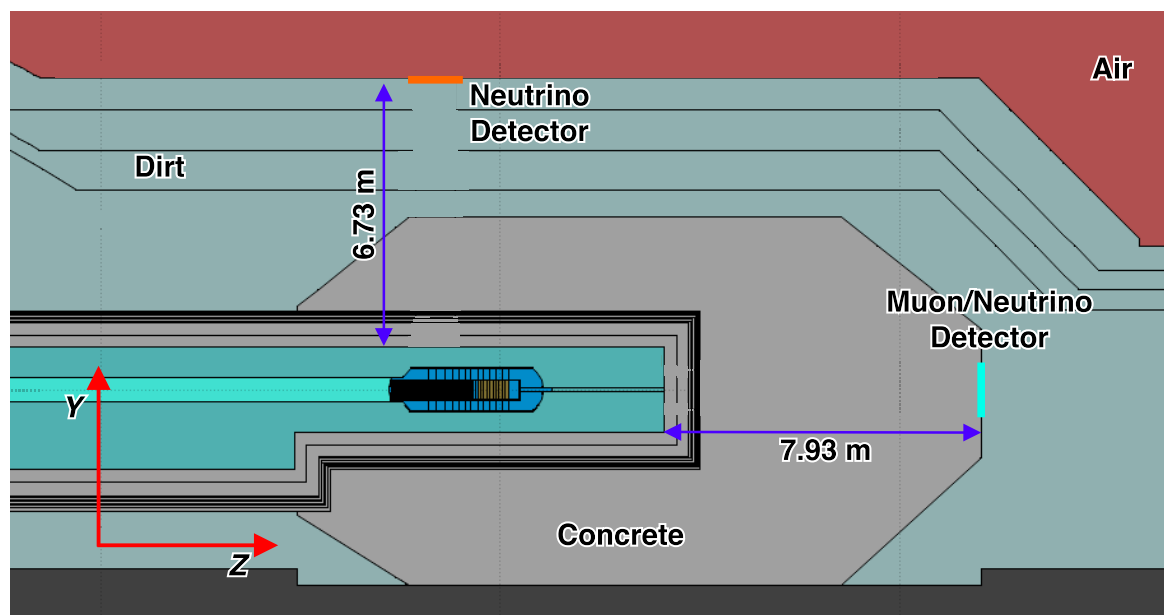


Figure 1. Scale side cross section of the Hall-A beam dump geometry with the two flux-detectors used in the simulations to evaluate the flux of secondary particles. Perpendicular to the beam dump, in orange, is shown the flux detector corresponding to the location of an hypothetical neutrino detector. Aluminum disks of beam dump inner core are shown in yellow. Downstream of the beam dump, immediately after the concrete vault, a hypothetical muon/neutrino detector's location is shown in light blue.

The input parameters used to run the program include all physics processes and a tuned set of biasing weights. As a reference, we considered a run time of 1 year corresponding to $\sim 10^{22}$ EOT. Simulations corresponding to such high statistics would require an unpractical time with the available

computing resources. To speed up the running time while preserving accuracy, biasing techniques were used to effectively reach the target statistics. Two biasing techniques provided by FLUKA were employed (an overview of biasing techniques in Monte Carlo simulations is described in Ref. [5]). The first, known as *surface splitting*, involves splitting a particle when it crosses two regions of increasing importance, as depicted in Figure 2. The second technique, referred to as *interaction length biasing*, involves a reduction in photon–nucleus interaction length, thereby increasing the number of particles produced, especially muons.

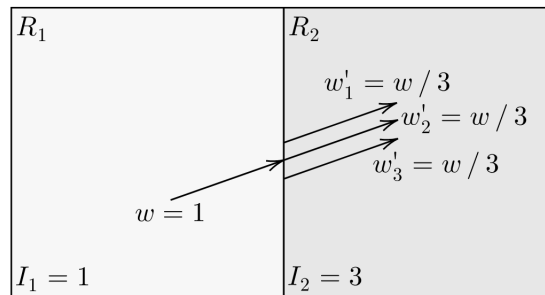


Figure 2. Surface splitting biasing mechanism scheme. A particle passing into a region with higher importance is split and given a weight equal to its initial weight divided by the importance of the current region.

The user FLUKA routines, written in FORTRAN and C++ programming languages, were used to generate a custom output file as a ROOT TTree [14]. This approach offers several advantages. Firstly, it facilitates the parallelization of the simulation across multiple CPUs, as the data can be easily merged at the end of the simulations. Secondly, it enhances flexibility in post-simulation analysis of results. Unlike the standard FLUKA scorers, which require predefined input settings, the TTree format allows data post-processing with no need to run the same simulations multiple times. Whenever a particle crosses the boundary between two selected regions, the following information is saved: crossing surface identifier, particle ID, statistical weight, total energy and momentum, crossing position vertex, direction (represented as direction cosine), parent particle ID, parent particle energy, production vertex, and production process identifier. The stored information is subsequently processed using dedicated ROOT scripts, written in Python, leveraging the pyROOT interface [15].

3.2. GEANT4

LDM can be produced by the interaction of standard model particles with ordinary matter. In this paper, we only consider DM particles produced by the interaction of the secondary muon beam with the BD and surrounding materials. (LDM produced in the direct interaction of the primary electron beam with the BD was studied and reported in Ref. [16]). LDM flux was computed using GEANT4 via the GEMC interface [17]. Hall-A BD geometry implemented in GEMC is shown in Figure 3.

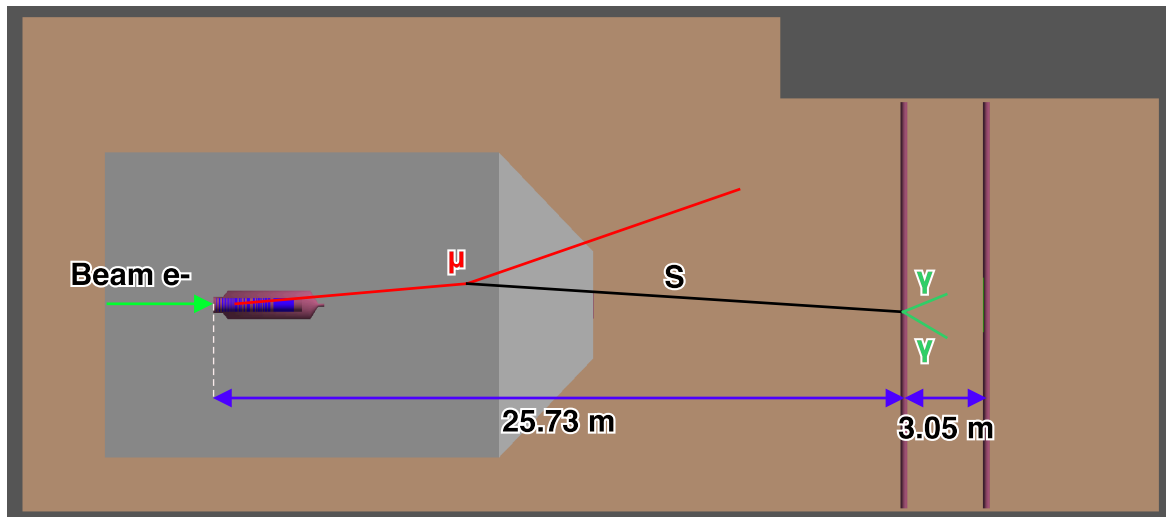


Figure 3. Hall-A BD and surrounding dirt implemented in GEMC. The BD vessel, shown in purple, contains Al foils, in blue. The concrete vault is shown in gray, while the dirt is shown in brown. Two existing 10" pipes installed ~ 26 m and ~ 29 m downstream of the dump [18] are shown in purple. A scheme of dark scalar production and decay is also presented.

The simulation procedure is divided into several steps. It starts by sampling muon features obtained with FLUKA simulations (see Section 4). The multi-dimensional distribution that includes three-momentum, production vertex, statistical weights, and total yield per electron on target (EOT) was converted in the LUND format (particle ID, vertex and momentum), and fed to GEMC. The interaction of muons with nuclei that produces a new hypothetical dark matter scalar particle S was added to the GEMC process list (details of the theoretical model are presented in Section 6). The process was implemented according to the prescription described in Ref. [19], with a more precise production cross section and subsequent propagation and decay [20]. The new class, `G4Scalar`, containing a `G4ParticleDefinition` instance to include the new S particle was implemented in GEMC libraries. The class initialization requires two parameters: the mass of the scalar and the coupling to standard model (SM). This allows one to dynamically set the particle properties at the beginning of the simulation. The LDM particle is then set to be unstable, with a lifetime that is analytically evaluated following Ref. [20]. A single decay channel ($S \rightarrow \gamma\gamma$) was implemented using the standard GEANT4 `G4PhaseSpaceDecayChannel` routine. In Section 6.1 (Section 6.2), we describe the main characteristics of LDM scalar flux produced by the interaction of the high-intensity 11 GeV (22 GeV) electron beam with the Hall-A BD. Finally, the expected sensitivity of a compact detector located ~ 29 m downstream of the BD as a function of the S mass and coupling constant is reported.

4. Secondary Muon Beams

High-intensity muon beams have applications in many research fields spanning from fundamental particle physics [21] to material science [22] and inspection and imaging [23]. In particular, the use of high-intensity GeV-energy muon beams could lead to the discovery of new light particles not predicted by the SM.

Most of the current [24–29] and planned [30–32] facilities produce muons as secondary particles via the decay of pions/kaons created by the interaction of an intense proton beam, typically of several MW power, with a heavy material target. A high-intensity multi-GeV electron beam hitting a thick target is likewise a copious source of muons. In this case, muons are produced via two classes of processes:

- Photo-production of π 's and K 's, which subsequently decay into muons;
- Direct $\mu^+\mu^-$ pair production.

In the latter, muons with energy to the order of the primary electron beam energy are produced through a two-step process. First, an electron radiates a γ in the nucleus field. Secondary particles are then photo-produced nearby. The production through a virtual photon exchange (direct electro-production) is instead negligible [33]. Radiated muons are strongly peaked in the forward direction with energy comparable to the primary beam energy. Instead, muons produced via decay in flight of photo-produced π 's and K 's show a lower energy spectrum. Monte Carlo simulations of muons produced by the interaction of CEBAF 11 GeV (22 GeV) e^- -beam with Hall-A BD are shown in Section 4.1 (Section 4.2). Distributions are shown for muons with energy greater than 100 MeV.

4.1. 11 GeV Electron Beam

To simulate the production and propagation of muons, $\sim 5 \times 10^8$ primary electrons with momentum $p_{e^-} = 11$ GeV were generated using the biasing technique described in Section 3.1 to reach the target statistics. Results are provided per EOT so that they can be easily extrapolated to 10^{22} EOT.

Momentum distributions of all muons produced in the BD resulting from the two production mechanisms (radiation and hadrons decay), are shown in Figure 4. The muon flux has been sampled at the boundary between the inner core of BD and the outer one. Decay in flight of π 's and K 's dominates muon production below 2 GeV, while pair productions dominate at higher energies.

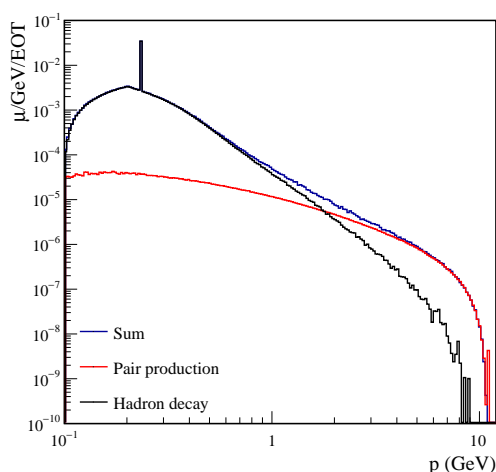


Figure 4. Momentum spectrum of muons at the boundary between the inner core of BD and the outer one with $p > 100$ MeV produced by 11 GeV (blue) electron beam. Pair production is shown in red and hadron decay is shown in black. The ratio between the integrated red and blue spectra is ~ 15 . The peak at 235 MeV is due to the kaon decay-at-rest process $K \rightarrow \mu + \nu_\mu$.

The kinetic energy distribution of muons produced by the 11 GeV CEBAF electron beam interacting with Hall-A BD is represented by the blue line in Figure 5. The flux was computed on a sampling plane (1 m^2) located 10 m downstream the beam dump and perpendicular to the primary e^- beam direction (corresponding to the light blue thick line in Figure 1). The resulting muon yield per EOT, integrated over $p_\mu > 100$ MeV, is $\sim 10^{-6}$. Therefore, for a primary e^- -beam current of $50 \mu\text{A}$, the corresponding muon rate is $\sim 10^8$ /s. These results show the advantage of secondary muon beams produced at multi-GeV electron BD facilities in comparison to the typical intensity of existing proton beam-produced muon beams with similar energies (the Fermilab accelerator complex, for example, can deliver a muon beam of about 10^7 /s at the so-called *magic momentum* of about 3 GeV [34]).

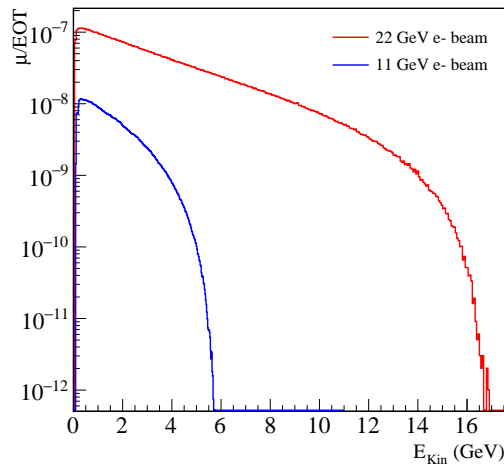


Figure 5. Muon energy distributions produced by an 11 GeV (blue line) and a 22 GeV (red line) CEBAF electron beam interacting with Hall-A BD.

Figure 6 (top) shows the muon spatial distribution and the direction (θ angle) of muons on the sampling surface: $\sim 50\%$ of the muons cross the plane within an area of roughly $50 \times 50 \text{ cm}^2$. The higher-energy muons are mostly produced in the forward direction, while the angular distribution becomes wider for lower energies.

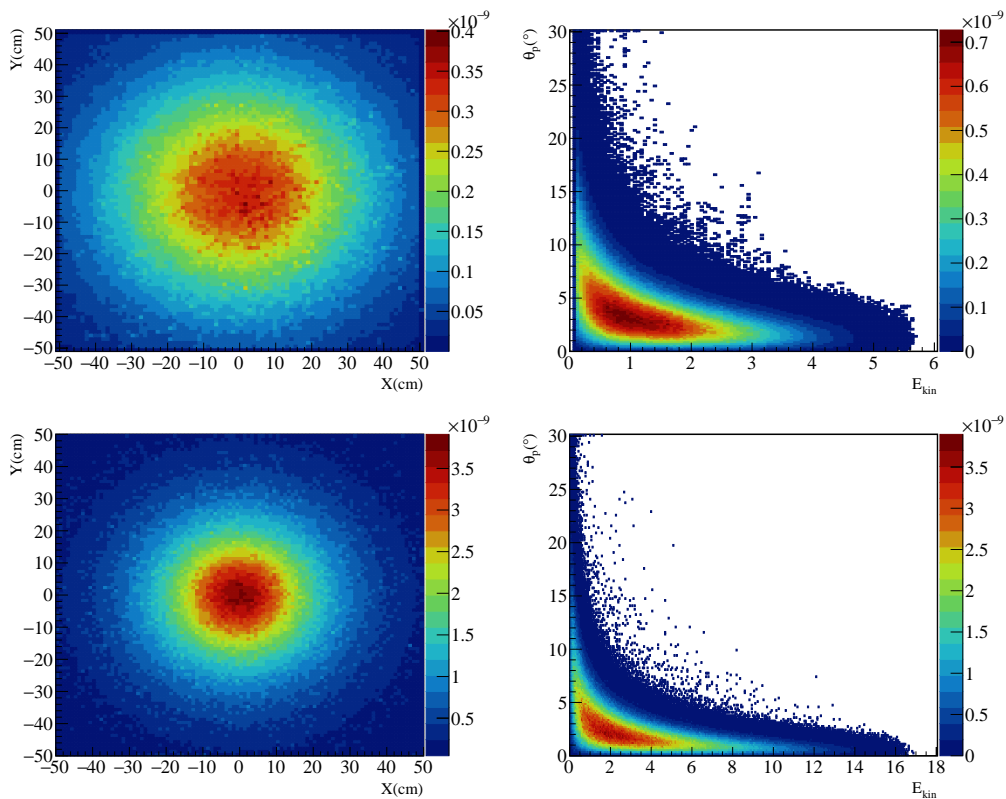


Figure 6. Upper left (lower left): spatial distribution of muons produced in the interaction of CEBAF 11 GeV (22 GeV) electron beam with Hall-A BD. Upper right (lower right): muon angular distribution as a function of energy for 11 GeV (22 GeV) electron beams.

4.2. 22 GeV Electron Beam

A similar simulation of $\sim 10^{10}$ EOT was performed assuming a CEBAF 22 GeV primary electron beam.

The resulting muon energy distribution is shown in Figure 5 with a red line. The spectrum remains Bremsstrahlung-like, similar to the 11 GeV case, but it covers an extended energy range (up to ~ 16 GeV) with an almost $\times 8$ yield. The spatial distribution (see Figure 6, bottom) results in being more forward-peaked, with the majority of muons lying on a narrower $\sim 40 \times 40$ cm² area.

The main characteristics of the muon beams produced by the interactions of 11 GeV and 22 GeV CEBAF electron beams with the Hall-A BD are summarized in Table 1.

Table 1. Summary of JLab secondary muon beam features.

Beam Energy	Flux /EOT		σ_x (cm)	σ_y (cm)
	100×100 cm ²	25×25 cm ²		
11 GeV	9.8×10^{-7}	1.5×10^{-7}	24.6	25.1
22 GeV	7.6×10^{-6}	1.9×10^{-6}	20.9	20.9

5. Secondary Neutrino Beams

Fission reactors and proton accelerators are currently the main source of neutrino beams. The reactors produce electron-type antineutrinos from fission fragment beta decay and are widely used in low-energy (\sim MeV) experiments. In accelerators, high-energy protons hit a target to generate short-lived hadrons (mainly π^\pm and K^\pm) that successively either decay in flight (DIF) or decay at rest (DAR) into neutrinos.

DAR neutrinos, mainly produced by spallation neutron sources [35], show an isotropic spatial distribution with an energy spectrum depending on the decay:

- $\pi^+ \rightarrow \mu^+ + \nu_\mu$, $E_\nu \sim 29.8$ MeV, almost monochromatic;
- $\mu^+ \rightarrow \bar{\nu}_\mu + \nu_e + e^+$, E_ν in the range 0–52.8 MeV;
- $K^+ \rightarrow \mu^+ + \nu_\mu$, $E_\nu \sim 236$ MeV, almost monochromatic.

DAR neutrinos are suitable for studying coherent elastic neutrino-nucleus scattering (CEvNS). This process, predicted a long time ago, has been only recently observed [36] and is a leading candidate for the study of non-standard (BSM) neutrino interactions [37].

Proton beam dump facilities are also used as high-intensity secondary neutrino beam generators [38,39].

In the following two sections, we will report the results of simulations of the 11 GeV (22 GeV) CEBAF electron beam interaction with the Hall-A BD, showing that this can be used as an efficient and high-intensity source of DAR neutrinos.

5.1. 11 GeV Electron Beam

To simulate the production and propagation of neutrinos produced by the interaction of the CEBAF 11 GeV electron beam with the Hall-A BD, the procedure described in Section 3.1 was used. Figure 7 shows the resulting neutrino energy spectrum. As anticipated in the previous section, a peak around 29.8 MeV and another peak 236 MeV related to π and k DAR, are clearly visible over a smooth background due to the muon decay and DIF events. The peak at 70 MeV has been tracked back to pion decay in electron and electronic neutrino. As expected, it is suppressed by four orders of magnitude with respect to the dominant allowed decay $\pi^+ \rightarrow \mu^+ + \nu_\mu$.

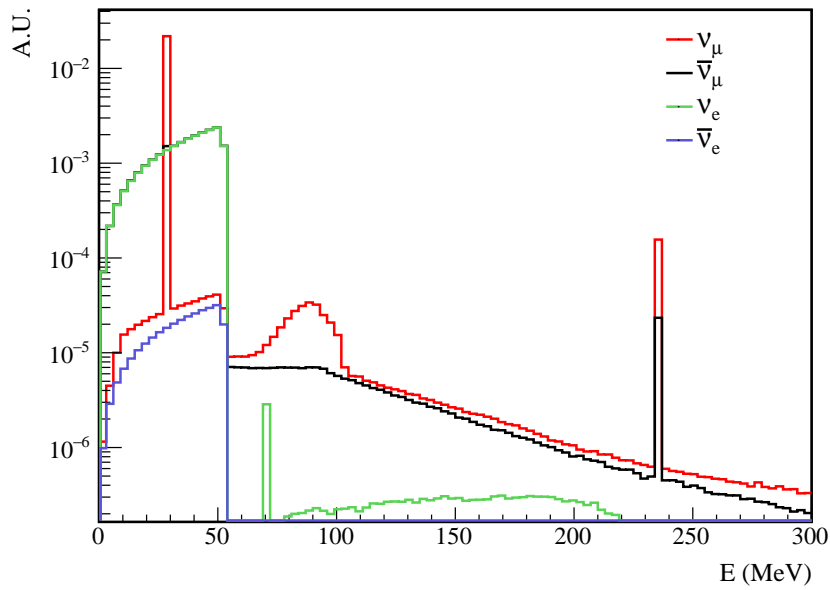


Figure 7. Neutrino energy spectrum produced by the interaction of the CEBAF 11 GeV e^- beam with the Hall-A BD. Each color corresponds to a different neutrino species, as the legend reports.

We studied the characteristics of the neutrino flux produced along the primary electron beam direction (on-axis) and perpendicular to it (off-axis). For the latter, we computed the flux on a 1 m^2 sampling plane located $\sim 10 \text{ m}$ above the dump corresponding to the ground level (orange surface in Figure 1). Results show that the off-axis ν energy spectrum (see Figure 8, left panel) is compatible with the spectrum of a DAR source. The overall neutrino flux in the energy range 0–100 MeV is $\sim 6.6 \times 10^{-5} \nu/\text{EOT}$, corresponding to 99% of the spectrum. Therefore, for an accumulated charge of 10^{22} EOT per year, an intense flux of $\sim 10^{18} \nu$, comparable to the integrated flux of the flagship DAR-neutrino facility SNS@Oak Ridge National Lab [35], is expected.

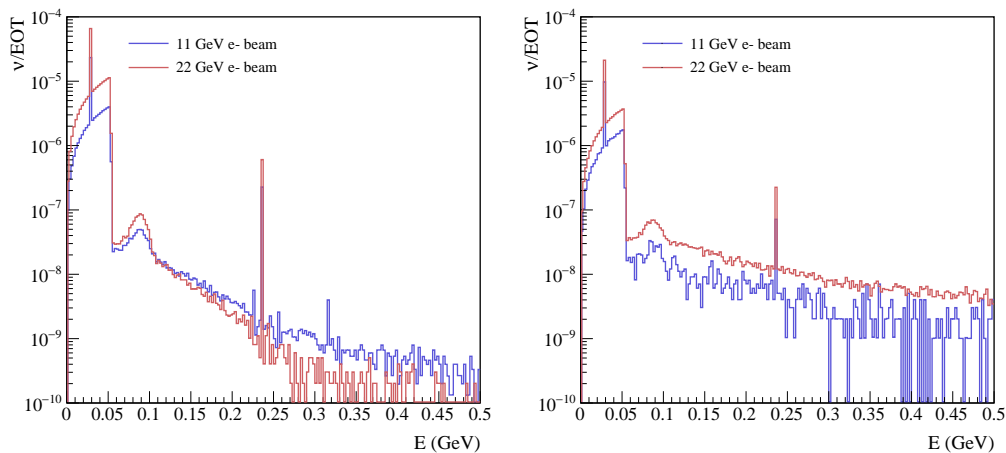


Figure 8. Energy distribution of off-axis (left panel) and on-axis (right panel) neutrinos produced by the interaction of 11 GeV (blue) and 22 GeV (red) CEBAF electron beams with the Hall-A BD.

Figure 8 (right panel) shows the energy distribution of on-axis neutrinos. The neutrino flux was sampled on a 1 m^2 -plane downstream of the BD at the exit surface of the concrete shielding (the same used for sampling muons in Section 4, corresponding to the light blue thick line in Figure 1). Even if the DAR contribution is dominant, a tiny but non-negligible part of the spectrum shows energies greater

than 100 MeV. The resulting on-axis neutrino flux in the energy range 0–500 MeV is $\sim 2.9 \times 10^{-5} \nu/\text{EOT}$, with the DAR part corresponding to $\sim 96\%$ of the overall yield.

5.2. 22 GeV Electron Beam

Similar to the previous paragraph, we evaluated the neutrino flux produced by the interaction of a primary 22 GeV e^- -beam with Hall-A BD. Figure 8 compares the on- and off-axis neutrino energy distributions produced by an 11 GeV and 22 GeV electron beam. They show a similar shape, with a yield difference of about a factor of two. More precisely, the results of simulations show an overall off-axis (on-axis) flux of $\sim 1.9 \times 10^{-4}$ (6.3×10^{-5}) neutrino/EOT in the energy range 0–500 MeV.

In Table 2 the characteristics of neutrino fluxes are summarized.

Table 2. Summary of JLab secondary neutrino beam features. Yields are obtained integrating the neutrino flux in the energy range 0–500 MeV.

Beam Energy	Off-Axis Flux [$\nu/\text{EOT}/\text{m}^2$]	On-Axis Flux [$\nu/\text{EOT}/\text{m}^2$]
11 GeV	6.7×10^{-5}	2.9×10^{-5}
22 GeV	1.9×10^{-4}	6.3×10^{-5}

6. Dark Matter Beams

Despite several years of research, the particle nature of dark matter remains one of the biggest endeavors in fundamental science (for a review, see [40]). Huge efforts have been spent in recent years into its identification, focusing on the search of weakly interacting massive particle candidates (WIMPs) with masses in the range 1 GeV–10 TeV. The lack of experimental evidences has motivated the interest toward sub-GeV light dark matter (LDM) where direct detection has a limited sensitivity [1,41–43]. To achieve the correct abundance inferred from astrophysical constraints, the interaction between LDM and SM states has to be mediated by a new gauge group that is light force carrier neutral under the standard model. The existence of the LDM would also bring theoretical predictions in agreement with observations [44,45] such as reconciling the persistent $\sim 4\sigma$ discrepancy in the anomalous magnetic moment of the muon [46,47].

The theoretical options for the inclusion of new interactions and particles in the SM are limited. A minimal list includes: the renormalizable vector portals mediated by a dark vector boson; scalar portals mediated by a new scalar mixing with the Higgs boson; and neutrino portal operators, mediated by a heavy neutral lepton. Vector and scalar portals are particularly motivated for a dark matter with mass in the MeV–GeV range. In parallel, a significant experimental activity has been performed to verify or falsify the different hypothesis. Data collected in previous experiments, optimized for different physics scopes, were re-analyzed within the above-mentioned theoretical frameworks, providing exclusion limits in the parameter space of the theories. New experiments, specifically designed to investigate the different options, have already collected data or are expected to run in the near future. We refer the interested reader to the *Feebly-interacting particles: FIPs 2022 Workshop Report* [48] for a comprehensive discussion about the possible LDM theoretical scenarios, the current experimental efforts, and a survey on the future proposals to detect LDM.

In this work, we focused on a minimal model that could explain the $(g-2)_\mu$ anomaly: a new *leptophilic* scalar dark matter state (*dark scalar* or *S*) that couples only to muons. A detailed description of the theoretical model is reported in Ref. [19,20] and the references therein. In this model, the main process responsible for *S* emission by an impinging muon on a fixed target is the so-called “radiative” production $\mu + N \rightarrow \mu + N + S$. The incident muon interacts with a target nucleus, *N*, by exchanging a photon, γ , and radiates the *S*.

For the mass range ($m_S < 2m_\mu$), S could only decay into two photons with a decay width, $\Gamma_{\gamma\gamma}$, which depends on the μ - S coupling constant, g_μ , and the ratio of muon to S masses, m_μ/m_S [20]:

$$\Gamma_{\gamma\gamma} = \frac{\alpha^2 m_S^3}{128\pi^3} \left| \frac{g_\mu}{m_\mu} \frac{4m_\mu^2}{m_S^2} \left[1 + \left(1 - \frac{4m_\mu^2}{m_S^2} \right) \arcsin^2 \left(\frac{4m_\mu^2}{m_S^2} \right)^{-1/2} \right] \right|^2 \quad (1)$$

Different experimental techniques can be used to search for muon-coupling light dark scalars. Among them, medium-energy electron beam dump experiments, providing an intense source of secondary muons, cover a broad area in the g_μ vs. m_S parameter space, as shown in Ref. [19]. As shown in Sections 4.1 and 4.2, muons are copiously produced by the interaction of the CEBAF electron beam with the Hall-A BD. They penetrate deeply into the dump and surrounding materials, losing energy mainly through ionization and, while traveling, may radiate a S particle.

In Sections 6.1 and 6.2, we present the characteristics of a hypothetical dark scalar S beam produced respectively by the interaction of a primary 11 GeV and 22 GeV electron beam with the Hall-A BD. For the former, a realistic evaluation of the background based on data collected at 10 GeV electron beam in the BDX-MINI experiment [49] was possible. This provided a solid ground to realistically evaluate the expected sensitivity of an experiment (sBDX-MINI), which uses a reduced version of the BDX detector [16]. Results are reported in Section 6.3. In the 22 GeV electron beam case, we did not evaluate the experimental sensitivity since a realistic background model was not available.

6.1. 11 GeV Electron Beam

In order to characterize the hypothetical dark scalar beam, $\sim 10^9 - 10^{11}$ muons were simulated using the biasing procedure described in Section 3.2. Simulations were performed assuming a fixed coupling constant $g_\mu = 3.87 \times 10^{-4}$ and m_S in the range 25 MeV–210 MeV. To keep the computational time reasonable, a further bias factor of 10^7 was introduced in FLUKA simulations.

Figure 9 shows results for the dark scalar beam obtained with an 11 GeV primary electron beam. The top panel shows the S spatial distribution on a sampling plane located 20 m downstream of the beam dump. The plot on the left was obtained assuming a dark scalar mass of $m_S = 50$ MeV, while the plot on the right refers to $m_S = 180$ MeV. The difference in the S beam spot size is due to a different fraction of energy transferred from the muon to the radiated S that increases for larger m_S (more energetic S corresponds to a smaller spatial spread).

The S energy spectrum is shown, for different m_S , on the top-left panel of Figure 10. The right column shows the S angular distribution with respect to the primary beam direction. All distributions are normalized to the number of S per EOT. The energy distribution for light scalar shows a peak at low energy, since for heavier scalar the out-going S takes a larger fraction of the muon energy. The kinematic of the produced S strongly depends on the mass: heavy S are mostly produced in the forward direction, while the angular distribution is wider for lighter S .

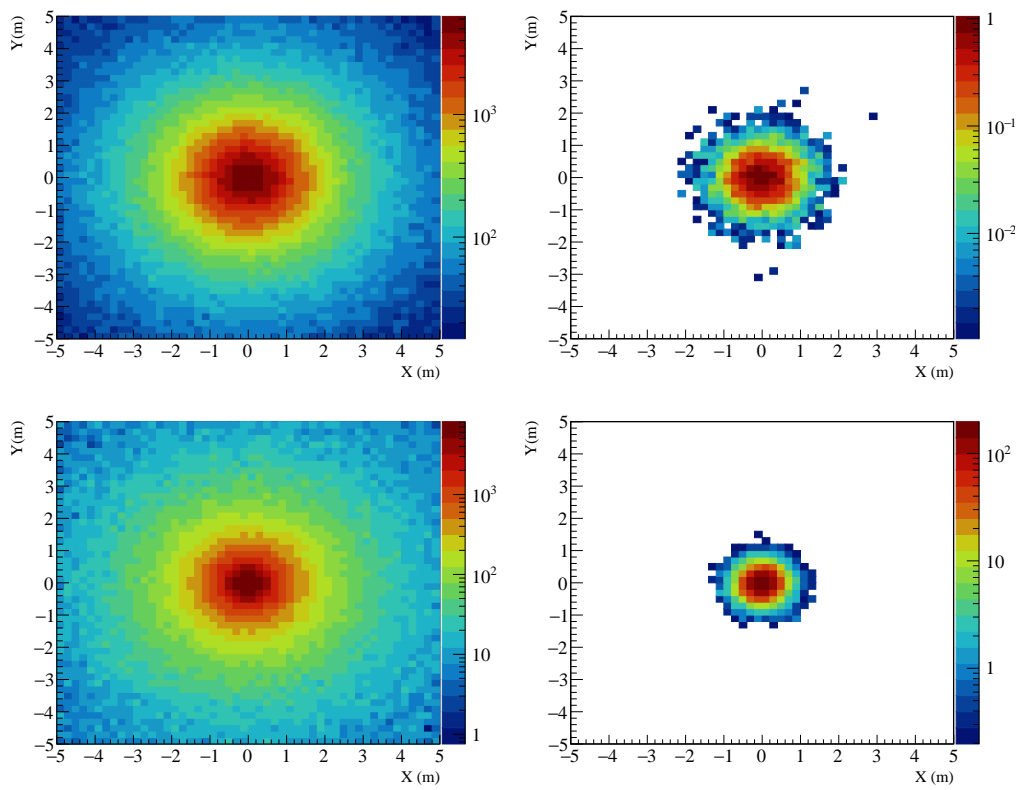


Figure 9. Spatial distributions of S sampled 20 m downstream of the beam dump. The top (bottom) row refers to an S beam generated by the 11 GeV (22 GeV) CEBAF electron beam. The beam spot size refers to $m_S = 50$ MeV (left) and $m_S = 180$ MeV (right).

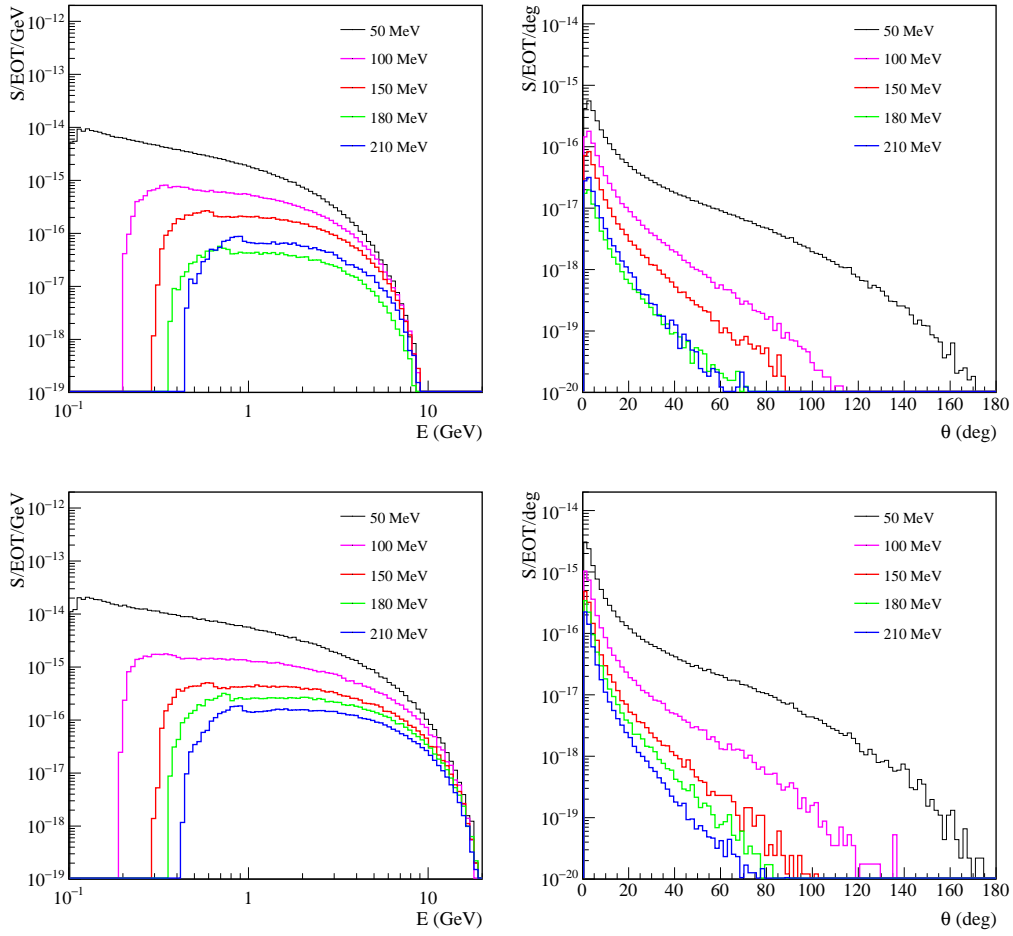


Figure 10. Energy (left) and angular (right) distributions of the dark scalar S for different masses. Results are shown for a primary 11 GeV electron beam (top) and 22 GeV (bottom).

6.2. 22 GeV Electron Beam

Simulations were performed using the same bias factor and coupling g_μ used for the 11 GeV electron beam case. The resulting beam spot size, energy, and angular distributions are shown in the bottom panels of Figures 9 and 10, respectively. They show a behavior similar to the 11 GeV case, with a more focused dark beam spot that covers an extended energy range. The S yield increases by a factor of 3–10, depending on the scalar mass.

Finally, Table 3 summarizes the expected S yield per EOT and beam spot size, sampled in a plane located 20 m downstream of the beam dump for an 11 and 22 GeV beam, and the two values of m_S .

Table 3. Summary of JLab scalar dark matter beam features.

Beam Energy (GeV)	$m_S = 50 \text{ MeV}$		$m_S = 180 \text{ MeV}$	
	S/EOT	σ (m)	S/EOT	σ (m)
11	5.27×10^{-15}	1.556	1.32×10^{-16}	0.488
22	1.90×10^{-14}	1.22	1.44×10^{-15}	0.304

6.3. Discovery Potential of sBDX-MINI Experiment

The two pipes already installed downstream of Hall-A BD could host a new experiment searching for the dark scalar particle S : sBDX-MINI. The same infrastructure was used for the BDX-MINI experiment [49]. In this section, we explored the sensitivity of a BDX-MINI-like experiment searching for S in the visible decay mode ($S \rightarrow \gamma\gamma$) with both gammas detected. The sBDX-MINI would make use of CEBAF 11 GeV e^- beam hitting the Hall-A BD running for about 1 year, with currents up to 75 μA (corresponding to an accumulated charge of 10^{22} EOT). We assumed a detector with a layout similar to BDX-MINI, with an almost cylindrical electromagnetic calorimeter with an 8 cm radius surrounded by a multi-layer veto system. To compensate for the limited pipe size ($10''$), we assumed a 2 m vertical length detector, roughly corresponding to 4 BDX-MINI detectors stacked. If we assume the current JLab setup, some muons produced by the 11 GeV beam interaction with the BD will reach the two pipes. To reduce this background, the detector was assumed to be located in the farthest well.

To evaluate the 90% C.L. exclusion limit in case of a null result, the formula $S^{UP} = 2.3 + 1.4\sqrt{B}$ [18], where S^{UP} is the upper limit on the number of signal events and B is the total number of background events, was used. The expected background was conservatively estimated using BDX-MINI beam-on (at 10 GeV e^- beam) and beam-off data [49] scaled for the volume of the sBDX-MINI detector. A background yield of $\sim 0.5 \times 10^{-12} \mu/\text{EOT}$ is estimated, requiring an energy threshold of 300 MeV. The upper limit on the number of signal events was then translated in an exclusion limit for g_μ coupling constant. The exclusion limit as a function of the S mass is shown in Figure 11. Although sBDX-MINI does not test unexplored regions in the g_μ vs. m_S parameter space, the sensitivity that could be achieved with such a limited-size detector suggests that a full version of the experiment (sBDX) would have significant sensitivity to a dark scalar particle.

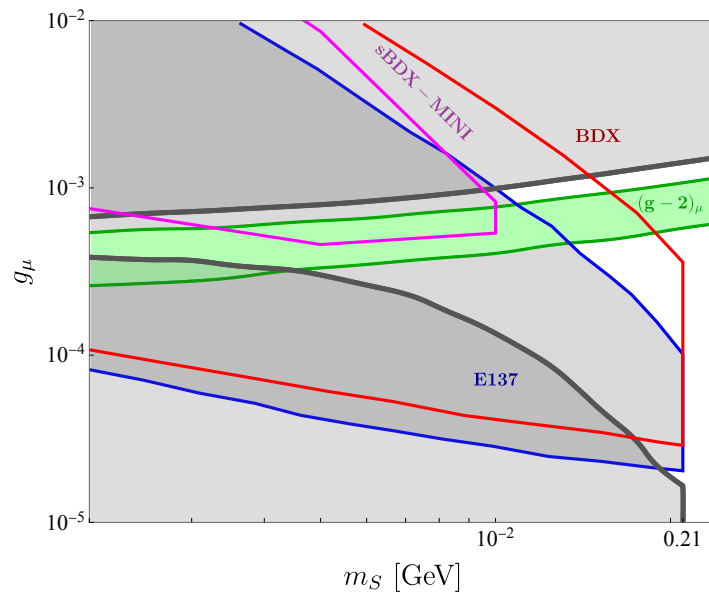


Figure 11. The 90% C.L. projection of the exclusion limit of sBDX-MINI. E137 exclusion limit (blue) and projection for BDX (red) sensitivity [19] are also reported. The gray area represents already excluded regions. The green band depicts the parameter combinations that could explain the $(g - 2)_\mu$ discrepancy. The sharp limit at ~ 0.21 GeV is related to the opening of $S \rightarrow \mu\mu$ competing decay channel.

7. Conclusions and Outlooks

In this paper, we demonstrated that existing high-intensity electron beam facilities may provide low-cost, opportunistic, high-intensity secondary particle beams that will broaden their scientific programs. We studied in detail the characteristics of muon, neutrino, and hypothetical light dark

matter beams obtained by the interaction of the CEBAF 11 GeV primary electron beam with the Jefferson Lab experimental Hall-A beam dump. High statistic simulations were performed with the FLUKA and GEANT4 toolkit. Results show: I) a secondary muon beam with a Bremsstrahlung-like energy spectrum extending up to 5 GeV would provide up to $\sim 10^{-6}$ μ /EOT, corresponding to a yield of 10^8 μ /s for an electron beam current of 50 μ A. II) a secondary neutrino beam with the typical decay-at-rest (DAR) energy spectrum would provide up to $\sim 7 \times 10^{-5}$ ν /EOT when integrated over a 1 m² detector located 10 m above the BD. Considering a delivered charge corresponding to 10^{22} EOT per year, the resulting integrated flux would be in the range of 10^{18} ν , comparable to dedicated flagship DAR- ν facilities such as SNS at ORNL. III) A (hypothetical) light dark matter *leptophilic* scalar particle beam that may shed light on the $(g - 2)_\mu$ discrepancy; this opportunity would pair with already approved experiments aiming to explore the dark sector, extending the BSM discovery potential of the Jefferson Lab.

In view of a possible upgrade to the beam energy, this study was repeated for a 22 GeV electron beam energy. Results showed that the CEBAF energy upgrade will be extremely beneficial for the secondary muon beam, extending the energy range up to 16 GeV and the muon flux by almost an order of magnitude. For the secondary neutrino beam, the DAR yield is expected to double, and, for the dark matter beam, the dark scalar particle yield would increase by up to an order of magnitude.

Funding

The work of C.L. and H.-S.J. is supported by the National Research Foundation of Korea (NRF) grant funded by the Korean government (MSIT) (No. NRF-2020R1F1A1077174). M.B., R.D.V. and T.V. are part of RAISE personnel. Their work is funded by the European Union—Next Generation EU and by the Ministry of University and Research (MUR), National Recovery and Resilience Plan (NRRP), Mission 4, Component 2, Investment 1.5, project “RAISE—Robotics and AI for Socio-economic Empowerment” (ECS00000035).

Acknowledgments: We gratefully acknowledge the support of the the Jefferson Lab Radiation Control Department. We would like to thank Jay Benesch for precious support to the secondary beam evaluation. The authors wish to thank also Luca Marsicano for invaluable support to the dark matter simulation.

Conflicts of Interest: No conflicts of interest

References

1. Battaglieri, M.; Belloni, A.; Chou, A.; Cushman, P.; Echenard, B.; Essig, R.; Estrada, J.; Feng, J.L.; Flaughner, B.; Fox, P.J.; et al. US Cosmic Visions: New Ideas in Dark Matter 2017: Community Report. In Proceedings of the U.S. Cosmic Visions: New Ideas in Dark Matter, College Park, MD, USA, 23–25 March 2017; p. 7. <https://doi.org/10.48550/arXiv.1707.04591>.
2. Sakaki, Y.; Michizono, S.; Terunuma, N.; Sanami, T. The potential of the ILC beam dump for high-intensity and large-area irradiation field with atmospheric-like neutrons and muons. *Nucl. Instrum. Methods Phys. Res. Sect. Accel. Spectrom. Detect. Assoc. Equip.* **2023**, *1050*, 168144. <https://doi.org/10.1016/j.nima.2023.168144>.
3. Accardi, A.; Achenbach, P.; Adhikari, D.; Afanasev, A.; Akondi, C.S.; Akopov, N.; Albaladejo, M.; Albataineh, H.; Albrecht, M.; Almeida-Zamora, B.; et al. Strong Interaction Physics at the Luminosity Frontier with 22 GeV Electrons at Jefferson Lab. *arXiv* **2023**, arXiv:2306.09360. <https://doi.org/10.48550/arXiv.2306.09360>.
4. Böhlen, T.T.; Cerutti, F.; Chin, M.P.W.; Fassò, A.; Ferrari, A.; Ortega, P.G.; Mairani, A.; Sala, P.R.; Smirnov, G.; Vlachoudis, V. The FLUKA Code: Developments and Challenges for High Energy and Medical Applications. *Nucl. Data Sheets* **2014**, *120*, 211–214. <https://doi.org/10.1016/j.nds.2014.07.049>.
5. Ferrari, A.; Sala, P.R.; Fassò, A.; Ranft, J. *FLUKA: A Multi-Particle Transport Code (Program Version 2005)*; CERN: Geneva, Switzerland, 2005. <https://doi.org/10.2172/877507>.
6. Agostinelli, S.; Allison, J.; Amako, K.A.; Apostolakis, J.; Araujo, H.; Arce, P.; Asai, M.; Axen, D.; Banerjee, S.; Barrand, G.J.N.I.; et al. GEANT4: A Simulation toolkit. *Nucl. Instrum. Methods Phys. Res. Sect. Accel. Spectrom. Detect. Assoc. Equip.* **2003**, *506*, 250–303. [https://doi.org/10.1016/S0168-9002\(03\)01368-8](https://doi.org/10.1016/S0168-9002(03)01368-8).

7. Battaglieri, M.; Bondi, M.; Celentano, A.; De Napoli, M.; De Vita, R.; Fegan, S.; Marsicano, L.; Ottonello, G.; Parodi, F.; Randazzo, N.; et al. Measurements of the muon flux produced by 10.6 GeV electrons in a beam dump. *Nucl. Instrum. Methods Phys. Res. Sect. Accel. Spectrom. Detect. Assoc. Equip.* **2019**, *925*, 116–122. <https://doi.org/10.1016/j.nima.2019.02.001>.
8. Battaglieri, M.; Bondi, M.; Celentano, A.; Cole, P.L.; De Napoli, M.; De Vita, R.; Marsicano, L.; Randazzo, N.; Smith, E.S.; Spreafico, M.; et al. Dark matter search with the BDX-MINI experiment. *Phys. Rev. D* **2022**, *106*, 072011. <https://doi.org/10.1103/PhysRevD.106.072011>.
9. The Official CERN FLUKA Website. 2023. Available online: <https://fluka.cern/> accessed on 1 January 2024.
10. Ahdida, C.; Bozzato, D.; Calzolari, D.; Cerutti, F.; Charitonidis, N.; Cimmino, A.; Coronetti, A.; D’Alessandro, G.L.; Donadon Savelle, A.; Esposito, L.S.; et al. New Capabilities of the FLUKA Multi-Purpose Code. *Front. Phys.* **2022**, *9*, 788253. <https://doi.org/10.3389/fphy.2021.788253>.
11. Battistoni, G.; Boehlen, T.; Cerutti, F.; Chin, P.W.; Esposito, L.S.; Fassò, A.; Ferrari, A.; Lechner, A.; Empl, A.; Mairani, A.; et al. Overview of the FLUKA code. *Ann. Nucl. Energy* **2015**, *82*, 10–18. <https://doi.org/10.1016/j.anucene.2014.11.007>.
12. Battistoni, G.; Ferrari, A.; Lantz, M.; Sala, P.R.; Smirnov, G.I. Generator of neutrino-nucleon interactions for the FLUKA based simulation code. *AIP Conf. Proc.* **2009**, *1189*, 343–346. <https://doi.org/10.1063/1.3274183>.
13. Kharashvili, M. *JLAB-TN-16-048*; Technical Report; 2016. <https://userweb.jlab.org/~battagli/bdx/16-048.pdf>
14. Brun, R.; Rademakers, F. ROOT—An object oriented data analysis framework. *Nucl. Instrum. Methods Phys. Res. Sect. Accel. Spectrom. Detect. Assoc. Equip.* **1997**, *389*, 81–86. [https://doi.org/10.1016/S0168-9002\(97\)00048-X](https://doi.org/10.1016/S0168-9002(97)00048-X).
15. Python Interface: PyROOT. 2023. Available online: <https://root.cern/manual/python/> accessed on 1 January 2024.
16. Battaglieri, M.; Bersani, A.; Caiffi, B.; Celentano, A.; De Vita, R.; Fanchini, E.; Marsicano, L.; Musico, P.; Osipenko, M.; Panza, F.; et al. Dark Matter Search in a Beam-Dump eXperiment (BDX) at Jefferson Lab. <https://doi.org/10.48550/arXiv.1607.01390>.
17. Ungaro, M.; Angelini, G.; Battaglieri, M.; Burkert, V.D.; Carman, D.S.; Chatagnon, P.; Contalbrigo, M.; Defurne, M.; De Vita, R.; Duran, B.; et al. The CLAS12 Geant4 simulation. *Nucl. Instrum. Methods Phys. Res. Sect. Accel. Spectrom. Detect. Assoc. Equip.* **2020**, *959*, 163422. <https://doi.org/10.1016/j.nima.2020.163422>.
18. Battaglieri, M.; Bersani, A.; Bracco, G.; Caiffi, B.; Celentano, A.; De Vita, R.; Marsicano, L.; Musico, P.; Panza, F.; Ripani, M.; et al. Dark matter search in a Beam-Dump eXperiment (BDX) at Jefferson Lab—2018 update to PR12-16-001. *arXiv* **2019**, arXiv.1712.01518. <https://doi.org/10.48550/arXiv.1712.01518>.
19. Marsicano, L.; Battaglieri, M.; Celentano, A.; De Vita, R.; Zhong, Y.M. Probing Leptophilic Dark Sectors at Electron Beam-Dump Facilities. *Phys. Rev. D* **2018**, *98*, 115022. <https://doi.org/10.1103/PhysRevD.98.115022>.
20. Chen, C.Y.; Pospelov, M.; Zhong, Y.M. Muon Beam Experiments to Probe the Dark Sector. *Phys. Rev. D* **2017**, *95*, 115005. <https://doi.org/10.1103/PhysRevD.95.115005>.
21. Aguillard, D.P.; Albahri, T.; Allspach, D.; Anisenkov, A.; Badgley, K.; Baeßler, S.; Bailey, I.; Bailey, L.; Baranov, V.A.; Barlas-Yucel, E.; et al. Measurement of the Positive Muon Anomalous Magnetic Moment to 0.20 ppm. *arXiv* **2023**, arXiv.2308.06230. <https://doi.org/10.48550/arXiv.2308.06230>.
22. Yaouanc, A.; de Réotier, P. *Muon Spin Rotation, Relaxation, and Resonance: Applications to Condensed Matter*; International Series of Monographs on Physics; OUP Oxford: Oxford, UK, 2011.
23. Das, S.; Tripathy, S.; Jagga, P.; Bhattacharya, P.; Majumdar, N.; Mukhopadhyay, S. Muography for Inspection of Civil Structures. *Instruments* **2022**, *6*, 77. <https://doi.org/10.3390/instruments6040077>.
24. μ SR Beamlines at TRIUMF. 2023. Available online: <https://cmms.triumf.ca/equip/muSRbeamlines.html> accessed on 1 January 2024.
25. Kiselev, D. PSI Muon Facilities. 2023. Available online: https://indico.cern.ch/event/1016248/contributions/4282379/attachments/2215080/3749805/Muoncollider_CERN24.3.2021.pdf accessed on 1 January 2024.
26. Miyake, Y.; Nishiyama, K.; Kawamura, N.; Strasser, P.; Makimura, S.; Koda, A.; Shimomura, K.; Fujimori, H.; Nakahara, K.; Kadono, R.; et al. J-PARC muon source, MUSE. *Nucl. Instrum. Methods Phys. Res. Sect. Accel. Spectrom. Detect. Assoc. Equip.* **2009**, *600*, 22–24. <https://doi.org/10.1016/j.nima.2008.11.016>.

27. ISIS Muon Source. 2023. Available online: <https://www.isis.stfc.ac.uk/Pages/Muons.aspx> accessed on 1 January 2024.
28. Ganguly, S. Muon Campus at Fermilab. *arXiv* **2022**, arXiv:2208.02889. <https://doi.org/10.48550/arXiv.2208.02889>.
29. M2 Beam Line. 2023. Available online: https://sba.web.cern.ch/sba/BeamsAndAreas/M2/M2_presentation.html accessed on 1 January 2024.
30. Williams, T.J.; MacDougall, G.J.; Riemer, B.W.; Gallmeier, F.X.; Louca, D. SEEMS: A Single Event Effects and Muon Spectroscopy facility at the Spallation Neutron Source. *Rev. Sci. Instrum.* **2023**, *94*, 033908. <https://doi.org/10.1063/5.0135721>.
31. Kim, Y.J. Current status of experimental facilities at RAON. *Nucl. Instrum. Methods Phys. Res. Sect. Beam Interact. Mater. Atoms* **2020**, *463*, 408–414. <https://doi.org/10.1016/j.nimb.2019.04.041>.
32. Chen, C.; Bao, Y.; Vassilopoulos, N. Design of the surface muon beamline of MELODY. *J. Phys. Conf. Ser.* **2023**, *2462*, 012027. <https://doi.org/10.1088/1742-6596/2462/1/012027>.
33. Cox, J.; Martin, F.; Perl, M.L.; Tan, T.H.; Toner, W.T.; Zipf, T.F.; Lakin, W.L. A high energy, small phase-space volume muon beam. *Nucl. Instrum. Methods* **1969**, *69*, 77–88. [https://doi.org/10.1016/0029-554X\(69\)90575-8](https://doi.org/10.1016/0029-554X(69)90575-8).
34. Chapelain, A. The Muon g-2 experiment at Fermilab. *EPJ Web Conf.* **2017**, *137*, 08001. <https://doi.org/10.1051/epjconf/201713708001>.
35. Akimov, D.; An, P.; Awe, C.; Barbeau, P.S.; Becker, B.; Belov, V.; Bernardi, I.; Blackston, M.A.; Bock, C.; Bolozdynya, A.; et al. Simulating the neutrino flux from the Spallation Neutron Source for the COHERENT experiment. *Phys. Rev. D* **2022**, *106*, 032003. <https://doi.org/10.1103/PhysRevD.106.032003>.
36. Akimov, D.; Albert, J.B.; An, P.; Awe, C.; Barbeau, P.S.; Becker, B.; Belov, V.; Bernardi, I.; Blackston, M.A.; Blokland, L.; et al. First Measurement of Coherent Elastic Neutrino-Nucleus Scattering on Argon. *Phys. Rev. Lett.* **2021**, *126*, 012002. <https://doi.org/10.1103/PhysRevLett.126.012002>.
37. Chatterjee, S.S.; Lavignac, S.; Miranda, O.G.; Sanchez Garcia, G. Constraining nonstandard interactions with coherent elastic neutrino-nucleus scattering at the European Spallation Source. *Phys. Rev. D* **2023**, *107*, 055019. <https://doi.org/10.1103/PhysRevD.107.055019>.
38. Athanassopoulos, C.; Auerbach, L.B.; Bauer, D.; Bolton, R.D.; Burman, R.L.; Cohen, I.; Caldwell, D.O.; Dieterle, B.D.; Donahue, J.B.; Eisner, A.M.; et al. The liquid scintillator neutrino detector and LAMPF neutrino source. *Nucl. Instrum. Methods Phys. Res. Sect. A: Accel. Spectrometers Detect. Assoc. Equip.* **1997**, *388*, 149–172. [https://doi.org/10.1016/S0168-9002\(96\)01155-2](https://doi.org/10.1016/S0168-9002(96)01155-2).
39. Aguilar-Arevalo, A.A.; Anderson, C.E.; Bazarko, A.O.; Brice, S.J.; Brown, B.C.; Bugel, L.; Cao, J.; Coney, L.; Conrad, J.M.; Cox, D.C.; et al. Neutrino flux prediction at MiniBooNE. *Phys. Rev. D* **2009**, *79*, 072002. <https://doi.org/10.1103/PhysRevD.79.072002>.
40. Bertone, G.; Hooper, D. History of dark matter. *Rev. Mod. Phys.* **2018**, *90*, 045002. <https://doi.org/10.1103/RevModPhys.90.045002>.
41. Krnjaic, G. Probing Light Thermal Dark-Matter With a Higgs Portal Mediator. *Phys. Rev. D* **2016**, *94*, 073009. <https://doi.org/10.1103/PhysRevD.94.073009>.
42. Fabbrichesi, M.; Gabrielli, E.; Lanfranchi, G. *The Physics of the Dark Photon—A Primer*; Springer International Publishing: Cham, Switzerland, 2020.
43. Filippi, A.; De Napoli, M. Searching in the dark: the hunt for the dark photon. *Rev. Phys.* **2020**, *5*, 100042. <https://doi.org/10.1016/j.revip.2020.100042>.
44. Liddle, A.R. *An Introduction to Modern Cosmology*; Wiley: Hoboken, NJ, USA, 2003.
45. Coy, R.; Hambye, T.; Tytgat, M.H.G.; Vanderheyden, L. Domain of thermal dark matter candidates. *Phys. Rev. D* **2021**, *104*, 055021. <https://doi.org/10.1103/PhysRevD.104.055021>.
46. Bennett, G.W.; Bousquet, B.; Brown, H.N.; Bunce, G.; Carey, R.M.; Cushman, P.; Danby, G.T.; Debevec, P.T.; Deile, M.; Deng, H.; et al. Measurement of the negative muon anomalous magnetic moment to 0.7 ppm. *Phys. Rev. Lett.* **2004**, *92*, 161802. <https://doi.org/10.1103/PhysRevLett.92.161802>.
47. Abi, B.; Albahri, T.; Al-Kilani, S.; Allspach, D.; Alonzi, L.P.; Anastasi, A.; Anisenkov, A.; Azfar, F.; Badgley, K.; Baessler, S.; et al. Measurement of the Positive Muon Anomalous Magnetic Moment to 0.46 ppm. *Phys. Rev. Lett.* **2021**, *126*, 141801. <https://doi.org/10.1103/PhysRevLett.126.141801>.
48. Antel, C.; Battaglieri, M.; Beacham, J.; Boehm, C.; Buchmüller, O.; Calore, F.; Carena, P.; Chauhan, B.; Cladè, P.; Coloma, P.; et al. Feebly Interacting Particles: FIPs 2022 workshop report. *Eur. Phys. J. C* **2023**, *83*, 1122. <https://doi.org/10.1140/epjc/s10052-023-12168-5>.

49. Battaglieri, M.; Bisio, P.; Bondí, M.; Celentano, A.; Cole, P.L.; De Napoli, M.; De Vita, R.; Marsicano, L.; Ottonello, G.; Parodi, F.; et al. The BDX-MINI detector for Light Dark Matter search at JLab. *Eur. Phys. J. C* **2021**, *81*, 164. <https://doi.org/10.1140/epjc/s10052-021-08957-5>.

© 2024 by the authors. Submitted to *Instruments* for open access publication under the terms and conditions of the Creative Commons Attribution (CC BY) license (<http://creativecommons.org/licenses/by/4.0/>).